European Journal of Mechanics / A Solids 114 (2025) 105729

Contents lists available at ScienceDirect

European Journal of Mechanics / A Solids

journal homepage: www.elsevier.com/locate/ejmsol

Full length article

Beating of eukaryotic flagella via Hopf bifurcation of a system of stalled molecular motors

Irene Anello [a], François Alouges [b], Antonio De Simone [a,c,*]

[a] MathLab, Scuola Internazionale Superiore di Studi Avanzati (SISSA), Via Bonomea 265, Trieste, 34136, Italy
[b] Centre Borelli, ENS Paris-Saclay, CNRS, Université Paris-Saclay and Institut Universitaire de France, 4, avenue des Sciences, Gif-sur-Yvette, 91190, France
[c] The BioRobotics Institute, Scuola Superiore Sant'Anna, Viale R. Piaggio 38, Pontedera (PI), 56025, Italy

ARTICLE INFO

Keywords:
Flagellar beating
Self-organization
Synchronization
Instability
Hopf bifurcation

ABSTRACT

The modeling of the beating of cilia and flagella in fluids is a particularly active field of study, given the biological relevance of these organelles. Various mathematical models have been proposed to represent the nonlinear dynamics of flagella, whose motion is powered by the work of molecular motors attached to filaments composing the axoneme. Here, we formulate and solve a nonlinear model of activation based on the sliding feedback mechanism, capturing the chemical and configurational changes of molecular motors driving axonemal motion. This multiscale model bridges microscopic motor dynamics with macroscopic flagellar motion, providing insight into the emergence of oscillatory beating. We validate the framework through linear stability analysis and fully nonlinear numerical simulations, showing the onset of spontaneous oscillations. To make the analysis more comprehensive, we compare our approach with two established sliding feedback models.

1. Introduction

Eukaryotic flagella exhibit characteristic beating patterns that enable propulsion in viscosity-dominated environments (Purcell, 1977; Lauga and Powers, 2009). This motion is powered by molecular motors that operate within the axoneme, a cytoskeletal structure conserved across species. Due to the importance of flagellar beating in various biological functions, understanding the mechanisms underlying motor coordination in the axoneme remains a central question in biophysics (Gaffney et al., 2011; Smith and Yang, 2004; Heuser et al., 2009; Velho Rodrigues et al., 2021; Moran et al., 2014).

The axoneme has a 9+2 structure, with nine microtubule doublets surrounding a central pair of microtubule doublets, as shown in Fig. 1. Each doublet consists of an A-tubule and a B-tubule. Between these doublets are molecular motor proteins (dyneins), which anchor their tails to the A-tubule while their heads are free to bind and release the B-tubule of the subsequent doublet (Lin and Nicastro, 2018). Since the microtubules are polar filaments, this ATP-powered binding action creates movement towards the minus end of the microtubule, resulting in the relative sliding of adjacent doublets. The axoneme is held together by passive elastic elements, such as radial spokes proteins and nexin cross-linkers, that, together with constraints at the base of the flagellum, transform the sliding of microtubules into bending of the axoneme.

A major focus of flagellar research is to understand how the forces generated by dynein acting at the microscopic scale coordinate to generate bending waves in the flagellum. Various mathematical models have been proposed to describe these interactions. A seminal study in this field was conducted by Machin (1958), who demonstrated the importance of internal activation within a flagellum as a mechanism to sustain oscillations. Interestingly, the equation first derived there has recently been rederived in Howard et al. (2022) using a molecular mechanics approach.

Different hypotheses on the interaction between motors and microtubule pairs lead to different feedback (or control) mechanisms, including sliding feedback (Brokaw, 1985, 1971; Gallagher et al., 2023; Geyer et al., 2022; Mondal et al., 2020), curvature feedback (Camalet and Jülicher, 2000; Riedel-Kruse et al., 2007; Oriola et al., 2017), and geometric clutch (Lindemann, 1994a,b; Bayly and Wilson, 2014). Within these models, feedback dynamics can be categorized as linear or nonlinear. Recently, nonlinear feedback dynamics has been shown to effectively describe the behavior of small flagella. In particular, while linear curvature feedback was initially considered ideal for fitting *Chlamydomonas* data (Sartori et al., 2016), the nonlinear sliding feedback model proposed by Cass and Bloomfield-Gadêlha (2023), which incorporates the attachment and detachment of antagonistic molecular motors, provides a better fit. A review of the three type of control models can be found in Sartori et al. (2016), Bayly and Wilson (2015).

* Corresponding author at: MathLab, Scuola Internazionale Superiore di Studi Avanzati (SISSA), Via Bonomea 265, Trieste, 34136, Italy.
E-mail addresses: desimone@sissa.it, a.desimone@santannapisa.it (A. De Simone).

https://doi.org/10.1016/j.euromechsol.2025.105729
Received 5 December 2024; Received in revised form 28 April 2025; Accepted 19 May 2025
Available online 18 June 2025

It is worth noting the existence of flagellar beating models that do not depend on mechanical feedback between motors and filaments but instead reproduce oscillatory flutter instabilities through an external follower force at the free end of an active filament (Clarke et al., 2024; Ling et al., 2018).

This study introduces a fully nonlinear model for flagellar waveforms which belongs to the family of sliding feedback models. This model couples a motor model obtained generalizing (Camalet and Jülicher, 2000; Jülicher and Prost, 1995) with the equation of motion for the flagellum modeled as a pair of filaments in a plane. We refer to this framework as the *μ-chemoEH* model.[1] Respecting the symmetric structure of the axoneme, this model aims to elucidate the tug-of-war scenario of antagonistic motors between filaments at the microscopic scale (Alouges et al., 2024). Additionally, it preserves the nonlinearity given by the transport term originally proposed in Jülicher and Prost (1995), Jülicher et al. (1997), which uses a nonlinear reaction–advection equation to model the distribution of molecular motors in space.

In this scenario, the beating of the eukaryotic flagellum is explained as an oscillatory (Hopf) bifurcation. When there is enough ATP, the stalled equilibrium configuration of molecular motors becomes unstable, and results in an oscillatory tug-of-war causing the alternating relative sliding of filaments. This work contains two main original contributions: firstly, the exploration of the two-state model in the nonlinear regime; and secondly, the investigation of the distribution of probabilities (that motors are bound/unbound) at the microscopic scale, when large bending deformations arise at the macroscopic scale.

In Section 2 we derive the equation of motion for the flagellum, which is modeled as two filaments that bend in a plane. Subsequently, we present three nonlinear chemical models: the μ-chemoEH, the cubic model (a simplified version of the former), and the chemoEH model (Oriola et al., 2017). Then, we conduct the linear analysis of the μ-chemoEH on long flagella and corroborate it with nonlinear simulations in the vicinity of the bifurcation point. Finally, we present and discuss a numerical comparison between the three models in the large-amplitude regime in the context of short flagella.

2. Nonlinear continuum equations

2.1. Kinematics

We use a simplified model for the axoneme, extensively used in literature (Camalet and Jülicher, 2000; Riedel-Kruse et al., 2007; Sartori et al., 2016; Cass and Bloomfield-Gadêlha, 2023), where its structure reduces to two microtubule doublets, as in Fig. 1.

The microtubules are modeled as a pair of elastic and inextensible filaments with the same length L and at fixed distance $a \ll L$. The centerline curve is parameterized as $s \to \mathbf{r}(s) \in \mathbb{R}^2$, where $s \in [0, L]$ is the arc-length. The two filaments are then parameterized through

$$\mathbf{r}_+(s) = \mathbf{r}(s) + a\mathbf{n}(s)/2, \quad \mathbf{r}_-(s) = \mathbf{r}(s) - a\mathbf{n}(s)/2. \tag{1}$$

The local tangent vector $\mathbf{t}(s)$ is

$$\mathbf{t}(s) = \mathbf{r}'(s). \tag{2}$$

From here on the symbol $'$ indicates the arc-length derivative ∂/∂_s. We denote by $\varphi(s)$ the angle between $\mathbf{t}(s)$ and the x-axis, such that $\mathbf{t} = (\cos\varphi, \sin\varphi)$, and by $\kappa(s) = \varphi'(s)$ the local curvature, such that $\mathbf{n}' = -\kappa\mathbf{t}$.

The bending of the pair of filaments is related to their relative sliding. The sliding displacement at position s along the neutral line is given by the difference between the total arc-lengths along the two filaments up to the points $\mathbf{r}_+(s)$ and $\mathbf{r}_-(s)$, namely

$$u(s) = u(0) - \int_0^s (|\mathbf{r}'_+(\sigma)| - |\mathbf{r}'_-(\sigma)|)\, d\sigma = u(0) + a(\varphi(s) - \varphi(0)), \tag{3}$$

where $u(0)$ is the basal sliding of one filament with respect to the other, and we consider it null for simplicity. We remark that in deducing the last identity (3) from the tangent and normal differential relations, we use the assumption $|\kappa| < 2/a$. Notice that by differentiating (3) we obtain

$$u' = a\varphi' = a\kappa. \tag{4}$$

2.2. Force and torque balance equations

The center filament is subject to internal forces $\mathbf{R}(s)$ and torque $M(s)$ that act at position s. The internal forces are balanced by the external hydrodynamic drag per unit length $\mathbf{f}_{fl}(s)$ through the local force balance equation

$$\mathbf{R}'(s) + \mathbf{f}_{fl}(s) = 0.$$

Since we are dealing with a slender body at low Reynolds number, we use the resistive force theory (RFT, Gray and Hancock (1955)) limit and express the external drag as a function of the centerline velocity $\mathbf{f}_{fl} = -\xi_n \dot{r}_n \mathbf{n} - \xi_t \dot{r}_t \mathbf{t}$, where ξ_n and ξ_t are the normal and tangential friction coefficients, while $\dot{r}_n$ and $\dot{r}_t$ are the normal and tangential components of the centerline velocity. The dot indicates the time derivative ∂/∂_t.

The local torque balance equation reads

$$M'(s) + T(s) + m(s) = 0, \tag{5}$$

where $M(s) = B\varphi'(s)$ is the bending moment proportional to the curvature with bending stiffness B, $T(s)$ is the shear stress, defined as

$$T(s) = \mathbf{R}(s) \cdot \mathbf{n}(s),$$

and $m(s)$ is the distributed moment density.

The position can be expressed in terms of the tangent angle by

$$\mathbf{r}(s,t) = \mathbf{r}(0,t) + \int_0^L \begin{pmatrix} \cos(\varphi(\sigma,t)) \\ \sin(\varphi(\sigma,t)) \end{pmatrix} d\sigma.$$

Moreover, the shear force can also be related to the tangent angle too by

$$T(s) = \left(\int_s^L \mathbf{f}_{fl}(\sigma)\, d\sigma \right) \cdot \mathbf{n}(s) + T(L).$$

Thus, assuming $m(s)$ is known, we can solve Eq. (5) for the tangent angle φ subject to appropriate boundary conditions. In this work, we consider clamped–free boundary conditions

$$\varphi(0) = 0, \quad \dot{\mathbf{r}}(0) = 0, \quad \mathbf{R}(L) = 0, \quad M(L) = 0. \tag{6}$$

2.3. Modeling activity

In the following, the distributed moment density m will be written as the product $m = af$, where $f = f(s,t)$ is a force density acting at position s in opposite directions on the two filaments. The force f is the sum of a passive part f_p and an active part f_a, $f = f_a + f_p$. The passive part is defined as the sum of an elastic and a viscous resistance to sliding, while the active part is an unknown of the problem. To close the system we need then a further equation for the active part, which will encode a feedback between the activity of the motors and the sliding u, or its velocity $\dot{u}$. In the following, we give the equations in this form

$$\begin{cases} \dot{X} = F(X, \dot{u}), \\ f_a = G(X, \dot{u}), \\ f_p = H(u, \dot{u}) \end{cases} \tag{7}$$

where F is a vector, G and H are scalars and X is a vector of variables related to the microscopic activity inside the flagellum. The active force f_a is exerted by the motors and powers the sliding u of the filaments which in turn determines their bending via Eq. (4). In the following sections, we describe three alternative versions of system (7).

[1] micro-chemo-Elasto-Hydrodynamic.

3. Chemo-mechanical models

3.1. The μ-chemoEH model

The activity inside the flagellum is modeled by considering molecular motors anchored to the upper filament ($\mathbf{r}_+$) as well as those anchored to the lower filament ($\mathbf{r}_-$), as shown in Fig. 1. Due to the polarity of the filaments, the molecular motors attach to and detach from the opposite filament relative to the one they are anchored to, with a directional motion to the minus end, creating sliding between the filaments. In this section we present the μ-chemoEH model, a generalization of the microscopic model illustrated in Camalet and Jülicher (2000), that relates the force generated by the motor-filament interaction to the relative sliding of the filaments. A description of this model is provided in Alouges et al. (2024), where the microscopic system was not coupled with the equations of motion for the filaments. In that work, the model was referred to as the two-row model for reasons that will become evident later.

Given the need to relate the macroscopic dynamics of microtubules and swimming flagella with the microscopic mechanism of motors, we introduce different scales. The largest one is defined by the arc-length $s \in [0, L]$, while the smallest is the uniform spacing δ between molecular motors. Within each small rod segment $(s, s+ds)$, we consider the presence of microscopic rigid segments of length ℓ, with $\delta \ll \ell \ll L$, reflecting the periodic microtubule structure and containing a large number N of motors. These segment, defined as tug-of-war units (Oriola et al., 2017), are described by the spatial coordinate $\xi \in [0, \ell]$. We focus on a specific point $s \in [0, L]$ and, for simplicity, we omit the dependence on s of all quantities in the rest of this subsection.

At the ℓ-scale, a stochastic two-state model is employed to model the activity of molecular motors. Each motor exists in one of two states: bound (state A) to the filament or unbound (state B) from it. Transitions between these states are driven by the consumption of chemical energy in the form of ATP. This energy is converted into mechanical work by going from the unbound state to the bound one. Each state has an associated potential, $W_A(\xi)$ and $W_B(\xi)$, whose difference is defined as $\Delta W = W_A - W_B$, while the switch between states is described by transition rates $\omega_{AB}(\xi) = \omega_A(\xi)$ and $\omega_{BA}(\xi) = \omega_B(\xi)$, representing the probability per unit time for a motor to go from state A to state B and vice versa. Since ATP drives these transitions, the rates depend on its concentration, denoted as Ω.

Referring to Fig. 1, the relative displacement of the upper filament with respect to the lower filament, is defined by $u(t)$, with velocity $\dot{u}(t)$. Let us define $P^+(\xi, t)$ as the probability density that a motor anchored to upper filament is in state A at position ξ and at time t. The motor force density per macroscopic unit length exerted by the motors anchored to the lower filament on the upper filament is defined as $-f^+$ and reads

$$f^+(t) = -\rho N \int_0^\ell P^+(\xi, t)\partial_\xi \Delta W(\xi) d\xi, \tag{8}$$

where ρ is the density of tug-of-war segments in the filament. Note that ρN is the number density of molecular motors along the flagellum, denoted in Camalet and Jülicher (2000) as ρ. We follow the force-sign convention of Howard et al. (2022). Similarly, $Q(\xi, t)$ is defined as the probability density that a motor anchored to the lower filament is in state A but located at ξ at time t. For simplicity, we introduce the notation $P^-(\xi + u(t), t) = Q(\xi, t)$, and we define as

$$f^-(t) = -\rho N \int_0^\ell P^-(\xi, t)\partial_\xi \Delta W(\xi) d\xi \tag{9}$$

the correspondent motor force for the lower filament.

The total active force density f_a felt by the upper filament is therefore

$$f_a = f^+ + (-f^-). \tag{10}$$

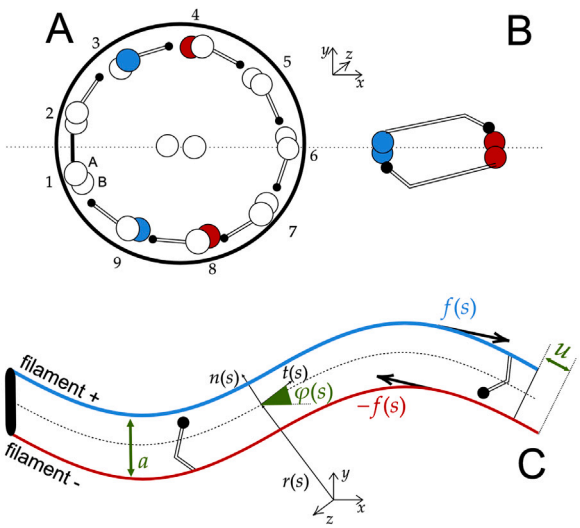

Fig. 1. From the axoneme to the two rows of molecular motors. (A) Cross section of the axoneme when viewed from the base to tip, with numbering taken from Sartori et al. (2016). (B) Projection of the axoneme onto its bending plane. (C) Flagellum composed by two filaments fixed at the base.

Viscous and elastic elements, represented by λ and K respectively, oppose the motion induced by the motors. The force on the upper filament can be then written as

$$f(t) = -2Ku(t) - 2\lambda\dot{u}(t) + f_a(t). \tag{11}$$

For $\xi \in [0, \ell]$ and $t > 0$, the complete PDE system describing the model is

$$\begin{cases} \dfrac{\partial P^+}{\partial t}(\xi, t) + \dot{u}(t)\dfrac{\partial P^+}{\partial \xi}(\xi, t) = -(\omega_A(\xi) + \omega_B(\xi))P^+(\xi, t) + \dfrac{\omega_B(\xi)}{\ell}, \\ \dfrac{\partial P^-}{\partial t}(\xi, t) - \dot{u}(t)\dfrac{\partial P^-}{\partial \xi}(\xi, t) = -(\omega_A(\xi) + \omega_B(\xi))P^-(\xi, t) + \dfrac{\omega_B(\xi)}{\ell}, \\ f(t) = -2\lambda\dot{u}(t) - 2Ku(t) - \rho N \int_0^\ell (P^+(\xi, t) - P^-(\xi, t))\partial_\xi \Delta W(\xi) d\xi. \end{cases} \tag{12}$$

The unfolding of the two filaments describing the flagellum (Figs. 1B and 1C), creates two rows of molecular motors, as can be seen in Fig. 2A. we have chosen this framework to describe the axoneme, rather than the simpler one-row model where the motors are attached only to the upper filament as in Camalet and Jülicher (2000), to capture the intuitive mechanics at play. When $\partial_\xi \Delta W < 0$ we have exactly the situation presented in Fig. 1(C), and the two rows of antagonistic motors compete through the forces, opposite in sign, f^+ and f^-. This tug-of-war framework implies that, when $\dot{u} = 0$ and the system is in equilibrium with probability density $P_0^+(\xi) = P_0^-(\xi)$, both motor rows are in a stalled configuration: each of them exerts a non-zero opposing force, with net active force equal to zero

$$0 = -\rho N \int_0^\ell P_0^+(\xi)\partial_\xi \Delta W(\xi) d\xi + \rho N \int_0^\ell P_0^-(\xi)\partial_\xi \Delta W(\xi) d\xi.$$

Instead, in the one-row model, at steady-state equilibrium, the stalled motors exert a non-zero net force:

$$-\rho N \int_0^\ell P_0(\xi)\partial_\xi \Delta W(\xi) d\xi,$$

where $P_0(\xi)$ is the equilibrium probability density of bound motors. This force causes filament displacement based on its stiffness K, breaking the symmetry of the ideal axoneme, where all microtubule doublets play identical roles. To restore symmetry, ΔW and P_0 can be chosen such that the net force at equilibrium is zero, as it was done in Camalet and Jülicher (2000).

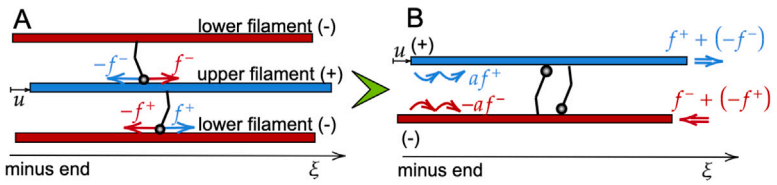

Fig. 2. (A) Unfolding of the flagellum's two-filament structure from Fig. 1. The red filaments indicate the same structure, identified as the lower filament (–). This is shown again in (B). Competing molecular motors exert a net force $f_a = f^+ - f^-$ on the upper filament, and the opposite force on the lower filament.

Exploiting standard assumptions (Camalet and Jülicher, 2000; Guérin et al., 2011b,a), we chose the potentials and the transition rates as

$$\begin{aligned} &\Delta W(\xi) = U\cos(2\pi\xi/\ell), \\ &\omega_A(\xi) + \omega_B(\xi) = \alpha, \\ &\omega_B(\xi) = \alpha\left(\eta + \tfrac{\Omega}{2\pi^2}\left(\cos(2\pi\xi/\ell) + \sin(2\pi\xi/\ell)\right)\right), \end{aligned} \tag{13}$$

where α is a rate constants, η is the average of the fraction of bounded motors

$$\eta = \frac{1}{\ell}\int_0^\ell \frac{\omega_B(\xi)}{\alpha}\, d\xi, \tag{14}$$

Ω represents the ATP concentration and U is the potential energy in a tug-of-war unit. All these coefficients are ξ-independent. Notably, the sum of the transition rates is uniform as in Camalet and Jülicher (2000) but they are not symmetric, in the sense of Guérin et al. (2011b), so that the μ-chemoEH can effectively symmetrize the system composed of the two filaments and the motors.

We expand the probability densities using Fourier series in space,

$$\begin{aligned} P^+(\xi,t) &= p_0(t) + \sum_{n>0}\left(p_n^+(t)\cos\frac{2n\pi\xi}{\ell} + q_n^+(t)\sin\frac{2n\pi\xi}{\ell}\right), \\ P^-(\xi,t) &= p_0(t) + \sum_{n>0}\left(p_n^-(t)\cos\frac{2n\pi\xi}{\ell} + q_n^-(t)\sin\frac{2n\pi\xi}{\ell}\right). \end{aligned} \tag{15}$$

If we plug (15) into the PDE system (12) we get an infinite number of ODE systems for the Fourier coefficients of $P^\pm$. We observe that the coupling between the probabilities dynamics and the force balance Eq. (11) takes place only for the first order coefficients, $n = 1$. This is therefore the only ODE that plays a role in the feedback between the motors' internal activity and the mechanical description of the flagella (see Appendix A.1).

For $n = 1$, we call $p^\pm = p_1^\pm$ and $q^\pm = q_1^\pm$ for simplicity and obtain

$$\begin{cases} \dot p^+(t) + \frac{2\pi}{\ell}\dot u(t) q^+(t) = -\alpha p^+(t) + \alpha\Omega/(2\pi^2\ell), \\ \dot q^+(t) - \frac{2\pi}{\ell}\dot u(t) p^+(t) = -\alpha q^+(t) + \alpha\Omega/(2\pi^2\ell), \\ \dot p^-(t) - \frac{2\pi}{\ell}\dot u(t) q^-(t) = -\alpha p^-(t) + \alpha\Omega/(2\pi^2\ell), \\ \dot q^-(t) + \frac{2\pi}{\ell}\dot u(t) p^-(t) = -\alpha q^-(t) + \alpha\Omega/(2\pi^2\ell), \\ f(t) = -2\lambda\dot u(t) - 2Ku(t) + \rho N\pi U\left(q^+(t) - q^-(t)\right). \end{cases} \tag{16}$$

In this case, system (7) reads $\underline{X} = (p^+, q^+, p^-, q^-)^T$,

$$F(\underline{X},\dot u) = -\alpha\underline{X} + \frac{2\pi}{\ell}\begin{pmatrix} 0 & -\dot u & 0 & 0 \\ \dot u & 0 & 0 & 0 \\ 0 & 0 & 0 & \dot u \\ 0 & 0 & -\dot u & 0 \end{pmatrix} X + \begin{pmatrix} \alpha\Omega/(2\pi^2\ell) \\ \alpha\Omega/(2\pi^2\ell) \\ \alpha\Omega/(2\pi^2\ell) \\ \alpha\Omega/(2\pi^2\ell) \end{pmatrix},$$

$G(X) = \rho N\pi U(\underline{X}\cdot\underline{e}_2 - \underline{X}\cdot\underline{e}_4)$ and $H(u,\dot u) = -2\lambda\dot u - 2Ku$.

3.2. The cubic model: an approximation

From the μ-chemoEH, we derive a differential equation that relates the active force f_a to the sliding velocity $\dot u$, embedding the motor dynamics probabilities into the resulting dynamics. This equation is referred to as the cubic model. The derivation partially follows (Jülicher et al., 1997) and the result is similar to the ODEs used in Sartori et al. (2016). Differentiating the active force $f_a = -\rho N\pi U(q^+ - q^-)$ with respect to time and substituting $\dot q^+$ and $\dot q^-$ using the second and fourth equations of system (16), we derive

$$\dot f_a = -\alpha f_a + \rho N\pi U\frac{2\pi}{\ell}\dot u(p^+ + p^-). \tag{17}$$

We focus on the first four equations of system (16) and assume a small perturbation around the steady state. We then have $\dot u = \varepsilon v$, with $|v| \le 1$, and we expand $p^\pm$ and $q^\pm$ as follows

$$p^\pm = \sum_{n\ge0}\tilde p_n^\pm\varepsilon^n, \quad q^\pm = \sum_{n\ge0}\tilde q_n^\pm\varepsilon^n,$$

where $\tilde p^\pm$ and $\tilde q^\pm$ satisfy

$$\begin{cases} 0 = -\alpha\tilde p_n^\pm \mp \frac{2\pi}{\ell}v\tilde q_{n-1}^\pm, \\ 0 = -\alpha\tilde q_n^\pm \pm \frac{2\pi}{\ell}v\tilde p_{n-1}^\pm, \end{cases} \tag{18}$$

for $n \ge 1$, and $\tilde p_0^\pm = \tilde q_0^\pm = \Omega/(2\pi^2\ell)$.

Here, we assume that the rate of change of v is small compared to α. As a result, the equations that determine the probabilities coefficients can be treated as quasi-static, with all variables adapting to v over time. In this context, setting the left-hand side of (18) to zero is reasonable, as the solution quickly converges to an equilibrium point determined by solving (18). From Eqs. (18), we recover the recursion relations

$$\tilde p_n^\pm = \mp\frac{2\pi}{\alpha\ell}v q_{n-1}^\pm, \quad \tilde q_n^\pm = \pm\frac{2\pi}{\alpha\ell}v p_{n-1}^\pm.$$

Substituting these into Eq. (17), and retaining terms up to order three in ε, we obtain the equilibrium relation

$$0 = -\alpha f_a + 2\rho N\Omega k_{cb}\varepsilon v\left(1 - \left(\frac{\varepsilon v}{\gamma}\right)^2\right) + O(\varepsilon^3), \tag{19}$$

where $\gamma = \frac{\ell\alpha}{2\pi}$ and $k_{cb} = U/\ell^2$. Thus, we approximate Eq. (17) by allowing the active force to evolve such that Eq. (19) holds at equilibrium. The idea behind this procedure is to simplify system (16) while preserving its linear characteristic. The coefficient γ is determined by the system's chemical properties, rather than selected *a posteriori*, as in Sartori et al. (2016).

System (7) is now defined by imposing $G(X,\dot u) = X$,

$$F(X,\dot u) = -\alpha f_a + 2\rho N k_{cb}\Omega\dot u(1 - \frac{\dot u^2}{\gamma^2}), \tag{20}$$

and $H(u,\dot u) = -2\lambda\dot u - 2Ku$. Notice that, in the frequency domain, Eq. (20) becomes the same as the nonlinear relation used in Hilfinger et al. (2009).

3.3. The chemoEH model

We present the third and last model, the chemoEH model (Oriola et al., 2017), based on the qualitative description made in Riedel-Kruse et al. (2007). The set up is the same as the one explained for the μ-chemoEH, where one fixes an arc-length $s \in [0, L]$ and considers a tug-of-war unit with two opposing filaments of length ℓ as shown in Fig. 1(C). In a tug-of-war unit, N is the total number of motors and $n^\pm(s,t)$ is the number of motors that are anchored to the $\pm$ filament and bound (state A) to the opposite filament. Let us define $F^\pm(s,t)$ as the load per motor each group of motors experiences caused by the action

of the antagonistic group. The load $F^{\pm}$ satisfies a linear force–velocity relationship where $F^{\pm} = F^{\pm}(\dot{u}) = \pm f_0(1 \mp \dot{u}/v_0)$. The stall force f_0 is defined as the absolute value of the load a motor experiences at stall, while v_0 is the relative velocity between the filaments at zero load. The external force is then balanced by an active part and a resistance to the sliding

$$\begin{aligned} f(s,t) &= \rho(n^+F^+ + n^-F^-) - Ku \\ &= \rho f_0\left((n^+ - n^-) - (n^+ + n^-)\frac{\dot{u}}{v_0}\right) - Ku. \end{aligned} \tag{21}$$

The evolution law for the quantities $n^{\pm}$ reads

$$\dot{n}^{\pm} = \pi_0(N - n^{\pm}) - \varepsilon_0 n^{\pm}\exp(\pm F^{\pm}/f_c), \tag{22}$$

where π_0 and ε_0 are constants rates and f_c is the characteristic unbinding force. In this model, the ratio $\bar{f} = f_0/f_c$ is held constant, while f_0 varies, reflecting the potential energy available to the motors, which is determined by the amount of ATP present in the system. The attachment rate π_0 (from unbound to bound state) is constant, while the detachment rate (from bound to unbound state) $\varepsilon_0 e^{\pm F^{\pm}(\dot{u})/f_c}$ varies with the filament velocity. In this case, system (7) reads $\underline{X} = (n^+, n^-)^T$,

$$F(\underline{X}, \dot{u}) = -\pi_0\underline{X} + \varepsilon_0 e^{\bar{f}}\begin{pmatrix} e^{-\bar{f}\frac{\dot{u}}{v_0}} & 0 \\ 0 & e^{\bar{f}\frac{\dot{u}}{v_0}} \end{pmatrix}\underline{X} + \begin{pmatrix} \pi_0 N \\ \pi_0 N \end{pmatrix},$$

$$G(\underline{X}, \dot{u}) = \rho(F^+, F^-)^T \cdot \underline{X} \text{ and } H(u) = -Ku.$$

3.3.1. Comparison between μ-chemoEH and chemoEH model

In the following, we highlight the main differences between the μ-chemoEH model and the chemoEH model, as they both aim to represent how the internal two-state chemistry of motors results in a sliding feedback mechanism.

Since the chemoEH model does not include the microscopic space variable ξ, it could be qualitatively interpreted as describing the average dynamics of the μ-chemoEH model over the tug-of-war unit. However, mathematical analysis of the two models demonstrates that the density of bound motors $n^{\pm}(t)/(N\ell)$ represents neither the average p_0 nor the first-order coefficients $p^{\pm}$ and $q^{\pm}$ of the Fourier expansion in (15). This is due to key differences, particularly in the transition rates between states. In the μ-chemoEH model, assumption (13) is such that the sum of the transition rates remains constant in both space and time, while in the chemoEH model this is generally not the case, except when $\dot{u} = 0$ and the sum is $\alpha_0 = \pi_0 + \varepsilon_0 e^{\bar{f}}$. Indeed, the derivation of the chemoEH model follows from Grill et al. (2005), where the main assumptions are that the unbind rate is load dependent and therefore velocity dependent, and that the motors have a detachment rate which is higher than the attachment one. These hypotheses are not compatible with the hypothesis of *uniform sum of transition rates* formulated in Guérin et al. (2011b), which holds when the two rates are almost uniform. Finally, in the chemoEH model there is no passive viscosity at play, $\lambda = 0$, but only an active viscosity, given by the term $(n^+ + n^-)\dot{u}/v_0$.

Following Jülicher (1999), we propose a comparison between the order of magnitude of the parameters appearing in the two models, using the difference of potentials defined in (13). We focus on the forces exerted on the upper filament: the force f^+ in Eq. (8) for the μ-chemoEH and the force $f^+_{cEH} := \rho n^+ F^+$ for the chemoEH model. When system (16) reaches equilibrium, the force in Eq. (8) becomes $f^+ = \rho NU\Omega/(2\pi\ell)$. In the chemoEH model, the corresponding equilibrium force is $f^+_{cEH} = n_{eq}\rho f_0$, where $n_{eq} = N\pi_0/(\pi_0 + \varepsilon_0 e^{\bar{f}})$, as defined in Appendix B. It follows that, to achieve comparable force magnitudes in the two models, the following relation must hold

$$f_0 \sim \Omega\frac{U}{2\pi\ell}\frac{n_{eq}}{N}. \tag{23}$$

Furthermore, when the two models describe the isolated axoneme, with $f = 0$, the linear analysis of the two ODE systems (A.2) and (B.1) reveal that the role of $n^+ - n^-$ is equivalent to the one of $q^+ - q^-$, implying a strict correlation between the two systems. Instead, the two models differ in their nonlinear part, as observed in Appendix B.

As noted in Cass and Bloomfield-Gadêlha (2023), in the chemoEH there are two characteristic times $\tau_0 = (\pi_0 + \varepsilon_0)^{-1}$ and $\alpha_0^{-1} = (\pi_0 + \varepsilon_0 e^{\bar{f}})^{-1}$. We chose the first one to be related to the characteristic dynein switching rate in the μ-chemoEH, by imposing $\alpha = \tau_0^{-1}$.

It is interesting to explore another commonly used set of potentials and transition rates, first introduced in Jülicher and Prost (1995) and later analyzed mathematically in Guérin et al. (2011b). In this case, W_B is modeled as a sawtooth potential, while ω_B is a rectangular function with its density concentrated at the minimum of W_B. Both W_A and ω_A are constant. This alternative chemical model is referred to as *localized transition rates*. It leads to a different nonlinear relationship between the active force and the sliding velocity at steady state. In practice, modifying the potential landscape significantly affects the nonlinear characteristics of the system. However, we chose not to pursue this model further, as the PDE in (12) cannot be reduced to a dynamical system, making a direct comparison with the chemoEH model difficult.

4. Linear stability analysis

In this section we perform the linear stability analysis of complete active axoneme by taking the μ-chemoEH (16) as the form of activation to be coupled with the scalar moment balance Eq. (5). Notice that the analysis would have been the same with the cubic model, which is introduced as an approximation of the μ-chemoEH nonlinearities.

The linearization of (5) around the equilibrium $\varphi = 0$ is

$$\xi_n\dot{\varphi}(s,t) + B\varphi''''(s,t) + af''(s,t) = 0. \tag{24}$$

This equation is obtained by differentiating twice Eq. (5), using the relation $(\dot{\mathbf{r}})' = \dot{\varphi}\mathbf{n}$, then applying the small deformation approximation to remove nonlinear terms. Assuming a linear perturbation of the form $f(s,t) = \tilde{f}(s)e^{\sigma t}$ and $\varphi(s,t) = \tilde{\varphi}(s)e^{\sigma t}$, where $\sigma = \mu + i\theta$, Eq. (24) becomes a fourth-order ODE for $\tilde{\varphi}(s)$

$$\xi_n\sigma\tilde{\varphi}(s) + B\tilde{\varphi}''''(s) - a^2\chi(\Omega,\sigma)\tilde{\varphi}''(s) = 0. \tag{25}$$

The coefficient

$$\chi(\Omega,\sigma) = 2\left(\lambda\sigma + K - \rho N k_{cb}\Omega\frac{\sigma}{(\alpha+\sigma)}\right), \tag{26}$$

with $k_{cb} = U/\ell^2$, is recovered from system (16) and relates the force f and the sliding u at the linear level in such a way that $\tilde{f} = -\chi(\Omega,\sigma)\tilde{u}$. Notice that the linear response coefficient (26) is twice the one defined in Camalet and Jülicher (2000).

We bring the system to a non-dimensional form by defining $\bar{s} = s/L$ and $\bar{t} = t\alpha$. The non-dimensional linear response coefficient becomes $\bar{\chi} = a^2L^2\chi/B$ and the ratio between viscous and elastic forces, called sperm number Sp, is defined as $\mathrm{Sp} = L(\xi_n\alpha/B)^{1/4}$. The non dimensional system of Eq. (25) together with clamped–free boundary conditions (6) becomes

$$\begin{aligned} &\bar{\sigma}\mathrm{Sp}^4\varphi + \varphi'''' - \bar{\chi}\varphi'' = 0, \\ &\varphi(0) = 0, \quad \varphi'''(0) - \bar{\chi}\varphi'(0) = 0, \\ &\varphi''(1) - \bar{\chi}\varphi(1) = 0, \quad \varphi'(1) = 0, \end{aligned} \tag{27}$$

where we dropped the $\tilde{}$ symbol on φ. Since the linearization of (5) implies that the tension is null, we only have four boundary conditions instead of six. The third equation of system (27) is derived from having zero velocity at the base, and hence $T'(0) = 0$.

The general solution to system (27) is $\varphi(s) = \sum_{j=1}^4 A_j e^{\beta_j\bar{s}}$, where β_j are the roots of the characteristic equation $\beta_j^4 - \bar{\chi}\beta_j^2 + \bar{\zeta} = 0$, while A_j are the amplitudes determined by the boundary conditions. The boundary conditions form a homogeneous system which admits non trivial solutions for the amplitudes A_j only if its determinant, defined as $\Lambda = \Lambda(\bar{\chi}, \bar{\sigma}; \Omega)$, is null.

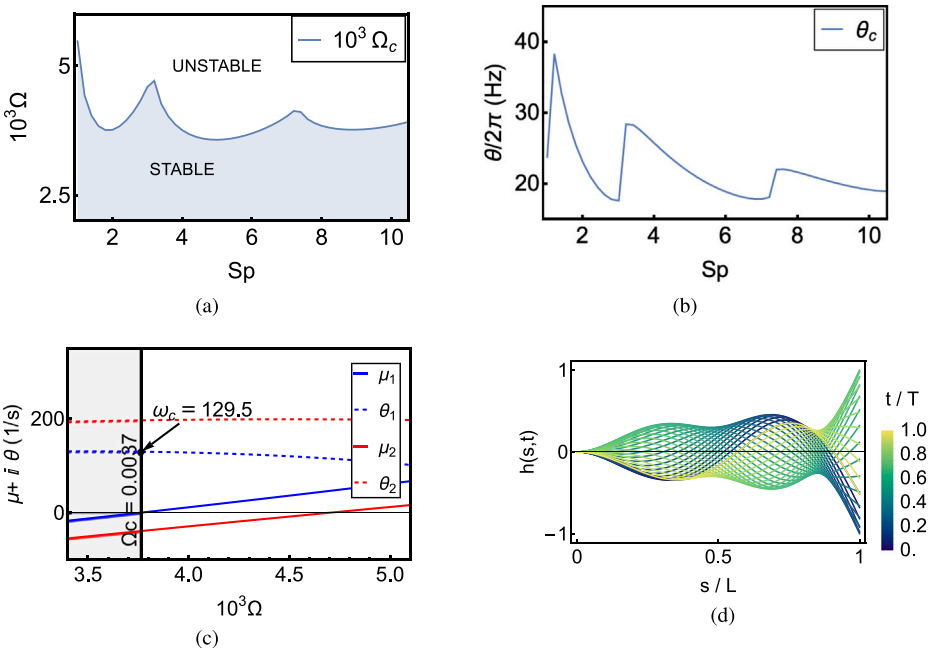

Fig. 3. Linear study of the μ-chemoEH applied to bull sperm parameters. (a), (b) Critical ATP concentration $10^3\Omega_c$ and critical frequency θ_c varying Sp. (c) Real (solid lines) and imaginary (dots, units are rad/s) parts of the first two modes varying the activation parameter $10^3\Omega$. (d) Transverse deformation $h(\bar{s})$ over one beating cycle. All the parameters are defined in Table 1.

For a fixed Ω, the equation $\Lambda(\bar{\sigma};\Omega)=0$ yields multiple solutions $\bar{\sigma}_n$, ordered by their real parts in such a way that $\mu_n > \mu_{n+1}$. We refer to these solutions as modes. This ensures that the first eigenvalue to cross the imaginary axis is $\bar{\sigma}_1$. At the critical ATP concentration $\Omega = \Omega_c$, defined by $\mu_1(\Omega_c)=0$ and $\theta_c = \theta_1(\Omega_c)$, the system is purely oscillatory.

4.1. Small Machin number

Consider an oscillatory ansatz $\varphi(s,t) = \tilde{\varphi}(s)e^{i\theta t}$ for the solution of Eq. (25). One can introduce an important non-dimensional quantity, the Machin number (Machin, 1958), defined as

$$\mathrm{Ma} = \frac{L}{\ell_{\mathrm{Ma}}}, \quad \ell_{\mathrm{Ma}} = \left(\frac{B}{\theta\xi_n}\right)^{1/4}, \tag{28}$$

with ℓ_{Ma} being the characteristic length of the system. When the system oscillates with frequency θ, the Machin number is therefore such that $M_a = \bar{\theta}^{\frac{1}{4}}\mathrm{Sp}$, where $\bar{\theta}$ is the dimensionless frequency. The Machin number is a natural parameter for studying systems where the oscillation frequency is known a-priori. In contrast, the sperm number is commonly used when the oscillation frequency emerges from an instability, and is an unknown of the problem.

If we consider small flagella such that $L \ll \ell_{\mathrm{Ma}}$, we can study the limit $\mathrm{Ma} \to 0$, which in turn implies $\theta \to 0$. In this case, the linear response coefficient reduces to the non-dimensional elastic term $\chi(\Omega, i\theta) \to K$. The non-dimensional linear equation for $\varphi(s)$ becomes $\varphi'''' - \mu_e\varphi'' = 0$, whose solution is a standing wave, suggesting that small Machin number flagella are not well-represented by a sliding feedback model.

A typical small Machin number flagellum is the *Chlamydomonas* ($L \approx 10\ \mu\mathrm{m}$), where experimental data in Sartori et al. (2016) reveal a critical frequency of $\theta_c = 2\pi \cdot 40\,\mathrm{s}^{-1}$ and therefore an estimated Machin number $\mathrm{Ma} \approx 2$, which the authors considered sufficiently small, in comparison with the bull sperm case ($L \approx 50\,\mu m$), where the ratio is instead $\mathrm{Ma} \approx 8$.

In Sartori et al. (2016), the sliding feedback model did not match well the experimental data for *Chlamydomonas* flagella. The authors attributed this discrepancy to the small ratio L/ℓ_{Ma} and the reasoning above. However a recent study (Cass and Bloomfield-Gadêlha, 2023), which developed an alternative nonlinear sliding feedback model, showed a better fit with the experimental data. This could be explained by the fact that nonlinearities are crucial to the system and/or that the Machin number is not small enough to justify the assumption. For this reason, we find useful to perform simulation of the μ-chemoEH sliding-feedback model also on short flagella.

5. The case of long flagella: numerical study

5.1. Near the bifurcation

In this chapter we present the case study of bull sperm, commonly proposed as a prototype for long flagella (Oriola et al., 2017; Bayly and Wilson, 2015). We use the μ-chemoEH model with the parameters outlined in Table 1. To facilitate the comparison with the literature we simulate the μ-chemoEH model by halving the motor force $f(t)$ defined in (16); in this way we obtain that the linear analysis matches the one in Camalet and Jülicher (2000).

The objectives of the following section are the following. First, we aim to confirm the agreement between the linear study and the fully nonlinear simulations for the μ-chemoEH model. Secondly, we investigate the coordination of molecular motors' probabilities appearing in Eq. (16). Lastly, we investigate how the nonlinear solution $\varphi(s,t)$ propagates in space and time by varying the sperm number (Sp) parameter.

The linear analysis for the two row model is carried out as presented in Section 4. To reproduce a beating frequency close to $20 \cdot 2\pi$ rad/s – which is the one shown in Riedel-Kruse et al. (2007) – we adjust the internal friction λ to 8 pN s/μm^2 (which is comparable to the one from Camalet and Jülicher (2000)). In Fig. 3(c) we observe the behavior of the real and imaginary part of the first two modes $\sigma_j = \mu_j + i\theta_j$ with $j = 1, 2$ as functions of the activation parameter Ω. The first mode crosses the imaginary axis with a critical frequency $\theta_c = 20.6$ Hz and at $\Omega_c \simeq 3.7 \times 10^{-3}$. Below this critical value all the modes are stable. Knowing the critical frequency, one can compute the Machin number (28) $\mathrm{Ma} = 7.4$, which in this case indicates that the system is in a high Machin number regime, where the sliding control model fits well the experimental data. Instead, the sperm number is $\mathrm{Sp} = 8.71$.

Table 1
Bull sperm parameters.

Param.	Definition	Units	Value	Ref.
L	Flagellum length	μm	58.3	Bayly and Wilson (2015)
B	Bending rigidity	pN μm^2	1700	Bayly and Wilson (2015)
a	Inter-filament distance	μm	0.185	Bayly and Wilson (2015)
ξ_n	Normal RFT coefficient	pN s/μm^2	0.0034	Bayly and Wilson (2015)
K	Internal elasticity	pN/μm^2	228	Sartori et al. (2016)
λ	Internal viscosity	pN s/μm^2	8	
α	Dynein rate constant	1/s	250	Bayly and Wilson (2015)
ℓ	Length of a tug-of-war cell	μm	1	Oriola et al. (2017)
ρ	Density of tug-of-war cells	1/μm	1	Oriola et al. (2017)
N	Motors in a tug-of-war cell	1	10^3	Oriola et al. (2017)
k_{cb}	Motor domain's stiffness	pN/μm	10^3	Camalet and Jülicher (2000)

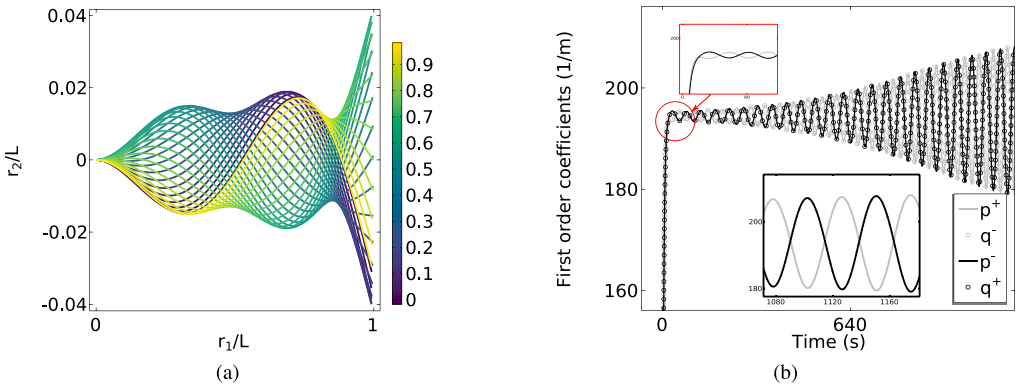

Fig. 4. Fully nonlinear simulations of the μ-chemoEH model applied to bull sperm parameters with $\varepsilon = 0.01$. (a) Deformed configuration during a beating cycle. The legend bar on the right indicates the time normalized over the period of oscillation t/T. (b) Oscillations in time of the first order for the probabilities $p^{\pm}(t)$ (solid gray and black line) and $q^{\pm}(t)$ (dotted black and gray line). The inlets are a close-up of the transient interval of time (in red) and one of the limit cycle regime (in black) where we only show $p^{\pm}$. All the parameters are defined in Table 1. (For interpretation of the references to color in this figure legend, the reader is referred to the web version of this article.)

In Figs. 3(a) and (b), we depict how the activation parameter Ω_c and the critical frequency θ_c respond to changes in the dimensionless ratio Sp. The stable region, in blue, corresponds to a non-oscillating system. These results align with the ones presented in Bayly and Wilson (2015). In practice, each value of the parameter Sp corresponds to a simulation with a distinct flagellum length L, determined by the formula $L = \mathrm{Sp} \cdot (\alpha \xi_n / B)^{-1/4}$; this length varies between $L \sim 6$ μm and $L \sim 60$ μm. Finally, in Fig. 3(d) we observe the behavior of the transverse deformation $\mathbf{r}(\bar{s}, \bar{t}) \cdot \mathbf{e}_2$ in the small amplitude regime, defined as

$$h(\bar{s}) = \int_0^{\bar{s}} \frac{\varphi(y, \bar{t})}{|\varphi(y, \bar{t})|}\, dy.$$

The angle φ is the solution of (27) corresponding to the critical bifurcation parameters $(\sigma, \Omega) = (i\theta_c, \Omega_c)$.

We now investigate the behavior of the fully nonlinear coupled system of equations given by (5) and (16), under clamped–free boundary conditions and in the time domain. Numerical simulations are conducted using COMSOL software (see Appendix C). We define the parameter $\varepsilon = |\Omega - \Omega_c|/\Omega_c$ to represent the relative deviation of the ATP concentration Ω from the critical bifurcation value Ω_c, determined through the linear analysis. To observe the bifurcated oscillatory solution, we apply an initial condition for the probabilities that slightly deviates from equilibrium:

$$p^{\pm}(0, s) = \frac{\beta}{\ell}(1 \pm 0.01), \quad q^{\pm}(0, s) = \frac{\beta}{\ell}(1 \mp 0.01).$$

In Fig. 4 we utilize the parameters in Table 1 to run simulations at the instability threshold, where $\varepsilon = 0.01$ and spontaneous oscillations take place. The deformed configuration of the flagellum during a beating cycle, defined as the curve $(r_1, r_2) = (\mathbf{r} \cdot \mathbf{e}_1, \mathbf{r} \cdot \mathbf{e}_2)$, is shown in Fig. 4(a) and closely matches the one of Fig. 3(d). The nonlinear simulations reproduce correctly the linear predictions of the critical activation Ω_c and of the frequency of oscillation θ_c.

Moreover, once the critical ATP threshold is reached, the first-order Fourier coefficients $p^{\pm}(t)$ and $q^{\pm}(t)$ of the probabilities (15) begin to oscillate in synchrony, as shown in Fig. 4(b). Specifically, we observe that $p^+ = q^-$ and $p^- = q^+$, with p^+ and q^+ exhibiting a phase shift of half a period relative to each other. The complete expression for the ξ-dependent probabilities $P^{\pm}(\xi, t)$ in Eq. (15) is given by

$$P^+(\xi, t) = p_0(t) + p^+(t) \cos \frac{2\pi\xi}{\ell} + q^+(t) \sin \frac{2\pi\xi}{\ell},$$
$$P^-(\xi, t) = p_0(t) + q^+(t) \cos \frac{2\pi\xi}{\ell} + p^+(t) \sin \frac{2\pi\xi}{\ell}.$$

Here, we find that $P^-(\xi, t) = -P^+\left(\frac{3}{4}\ell - \xi, t\right)$, implying a spatial phase shift of three-quarters of a period.

To conclude this section, we present nonlinear simulations for the bull sperm with $\varepsilon = 0.5$, which is close enough to the bifurcation. We observe a typical known behavior in flagella (Machin, 1958): by increasing the parameter Sp, the traveling wave velocity increases. In Fig. 5 the kymographs of the tangent angle $\varphi(s, t)$ are plotted against the non-dimensional flagellum length and over three periods of oscillations. The total length of the flagellum is varied by imposing different values of sperm number. When Sp=1 the viscous and bending forces are of comparable magnitude, and we observe almost standing waves: the flagellum does not generate any propulsion in the fluid. The more the viscous forces overcome the bending ones, the more we observe retrograde (tip to base) traveling waves with a significant speed.

5.2. Away from the bifurcation: comparison with the cubic model

In this section, we present a comparison between the μ-chemoEH model (Fig. 6(a)) and the cubic model (Fig. 6(b)), in the regime of large-amplitude deformations. We recall that the latter is derived from the former by means of an expansion analysis in the vicinity of the equilibrium point of system (16).

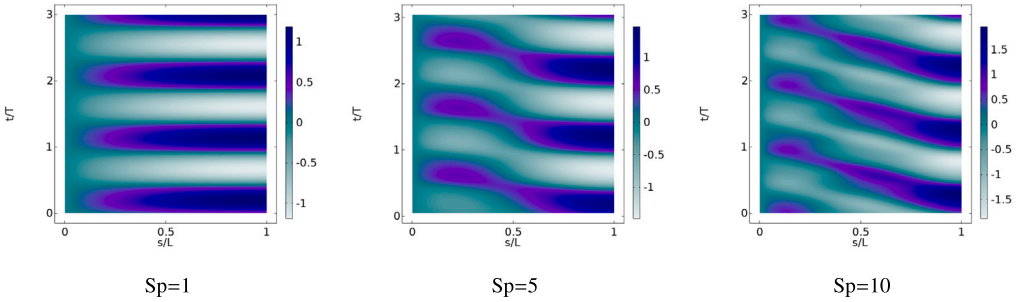

Fig. 5. Fully nonlinear simulations: kymographs of the tangent angle φ varying the sperm number Sp $\in \{1, 5, 10\}$. The legend bar on the right indicates the amplitude of φ. The tangent angle is plotted over the dimensionless arc-length and three period of oscillations. The wave speed increases by increasing Sp, going from a nearly standing wave to a traveling wave. All the parameters, except the length L, are defined in Table 1.

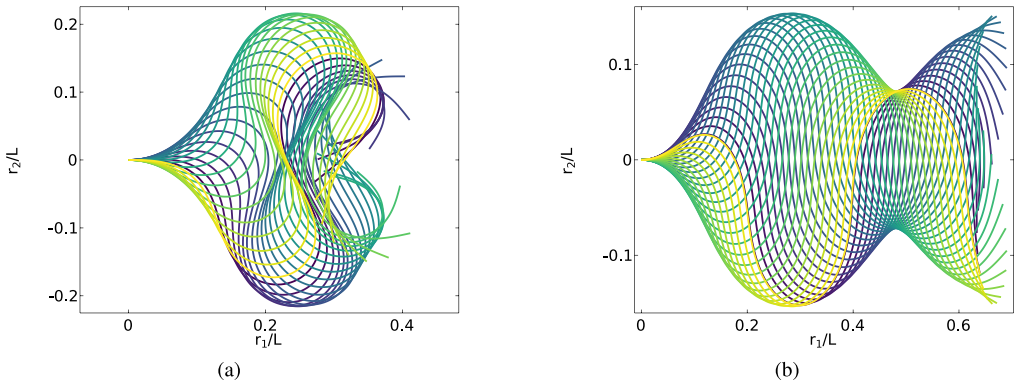

Fig. 6. Fully nonlinear simulations of the deformed configuration of bull sperm throughout a beating cycle. (a) The μ-chemoEH at $\varepsilon = 2$ and (b) the cubic model at $\varepsilon = 4$. Parameters in Table 1.

The μ-chemoEH model exhibits a greater sensitivity to the ε parameter than the cubic model. Even for the same small value of ε, the μ-chemoEH flagellum shows a larger deviation from the straight equilibrium configuration compared to the cubic model. This trend holds even for larger values of ε, which is why we present the waveform for $\varepsilon = 2$ in the case of the μ-chemoEH model and for $\varepsilon = 4$ for the cubic model. As shown in Fig. 6, the distinction is apparent: in the μ-chemoEH, the nonlinear terms are such that the flagellum exhibits more complex deformations with respect to the cubic model.

6. The case of short flagella: numerical study

6.1. Comparison between the three models

In the following chapter we focus on the results of nonlinear simulations of *Chlamydomonas*, using the parameters in Table 2. The parameters are chosen on the basis of previous works, with some adjustment to make the models more comparable. Recall that the dynein switching rate α is related with the characteristic time of the chemoEH model τ_0 as $\alpha = \tau_0^{-1}$. The internal elastic constant K is defined in such a way that $a^2K = 90$ pN, and the velocity $v_0 = 60$ μm/s is such that $\zeta = a/(\tau_0 v_0) = 0.4$; both of these choices were made to be close to the range of parameters used for the short flagella in Cass and Bloomfield-Gadêlha (2023). In the two-row model, the parameter η does not influence the computation of the active force f_a (10) because it only appears in the average p_0 of $P^{\pm}$. Since p_0 cancels out during the calculation of f_a, η has no effect on coupled system. In contrast, in the chemoEH model, the rates π_0 and ε_0 depend explicitly on η, making it an essential parameter in the formulation of the model. Once the parameter setting is defined, by gradually increasing the distance ε from the instability, we compare the results given by three different nonlinear model for flagellar beating activation: the μ-chemoEH, the chemoEH model and the cubic model.

The linear analysis gives the bifurcation values: for the μ-chemoEH and cubic model the onset of oscillation is at $\Omega_c = 0.0384$, while for the chemoEH we have $f_0 = 10.9$ pN. Therefore, the term given on the right side of the relation (23) is 51.3 pN, which makes the order of magnitude comparable.

We start close to the instability, with $\varepsilon = 0.01$, and then grow further away from it. In all of the following cases we analyze the system once it has entered its limit cycle. We observe that the μ-chemoEH waveforms, even for small distances ε from equilibrium, significantly deviate from the straight equilibrium state. Instead, the other two models show less sensitivity to the bifurcation parameter. This is noticeable in Fig. 7(a), where the transverse deformation is almost ten times larger than the ones in Fig. 7(b) and (c). The same observation applies to the maximum amplitude of the active force f_a, where, for both the μ-chemoEH and the cubic model, we considered $f(t)/2$ as the total motor force. In the second row of Fig. 7, we plot the active force versus the sliding velocity when the system enters its limit cycle for different arc-lengths, $s \in \{0.2L, 0.5L, 0.8L, L\}$. While they all have anticlockwise direction, we can observe that the amplitude of the active force, along with the velocity amplitude, is roughly ten times greater for the μ-chemoEH compared to the chemoEH model and the cubic model. The graphs confirm the existence of oscillations around the zero equilibrium point. The wave forms in the kymograph Fig. 7((g), (h), (i)) are similar, showing wave propagation from tip ($s = L$) to base ($s = 0$). Qualitatively, in all three models, the tangent angle $\varphi(s, t)$, deviates little from a sinusoidal shape, with the active force that grows gradually from base to tip. The critical frequencies are the following $\theta_c = 75.6$ Hz for the μ-chemoEH and cubic model, while $\theta_c = 80.2$ Hz for the chemoEH model.

When increasing the bifurcation value we observe different nonlinear behaviors depending on the model. Notice that to have comparable deformed configuration, we had to stop at $\varepsilon = 0.15$ for the μ-chemoEH, at $\varepsilon = 1.2$ for the cubic model and at $\varepsilon = 2$ for the chemoEH model, as shown in Fig. 8. For the μ-chemoEH, even at $\varepsilon = 1$, simulations show that the filaments start to twist on themselves.

Table 2
Chlamydomonas parameters for the μ-chemoEH/cubic model and for the chemoEH model.

	Param.	Definition	Units	Value	Ref.
All	L	Flagellum length	μm	12	Sartori et al. (2016)
	B	Bending rigidity	pN μm^2	840	Cass and Bloomfield-Gadêlha (2023)
	a	Inter-filament distance	μm	0.06	Sartori et al. (2016)
	ξ_n	Normal RFT coefficient	pN s/μm^2	0.0034	Sartori et al. (2016)
	K	Internal elasticity	pN/μm^2	25×10^3	
	α	Dynein rate constant	s$^-$1	200	
	ℓ	Length of a tug-of-war cell	μm	1	Oriola et al. (2017)
	ρ	Density of tug-of-war cells	μm^{-1}	1	Oriola et al. (2017)
	N	Motors in a tug-of-war cell	1	10^3	Oriola et al. (2017)
μ-chemoEH	λ	Internal viscosity	pN s/μm^2	4	
	k_{cb}	Motor domain stiffness	pN/μm	10^3	Camalet and Jülicher (2000)
chemoEH	v_0	Velocity at zero load	μm/s	60	
	$\bar{f}$	f_c/f_0	1	2	Oriola et al. (2017)
	η	Average of bound motors	1	0.5	

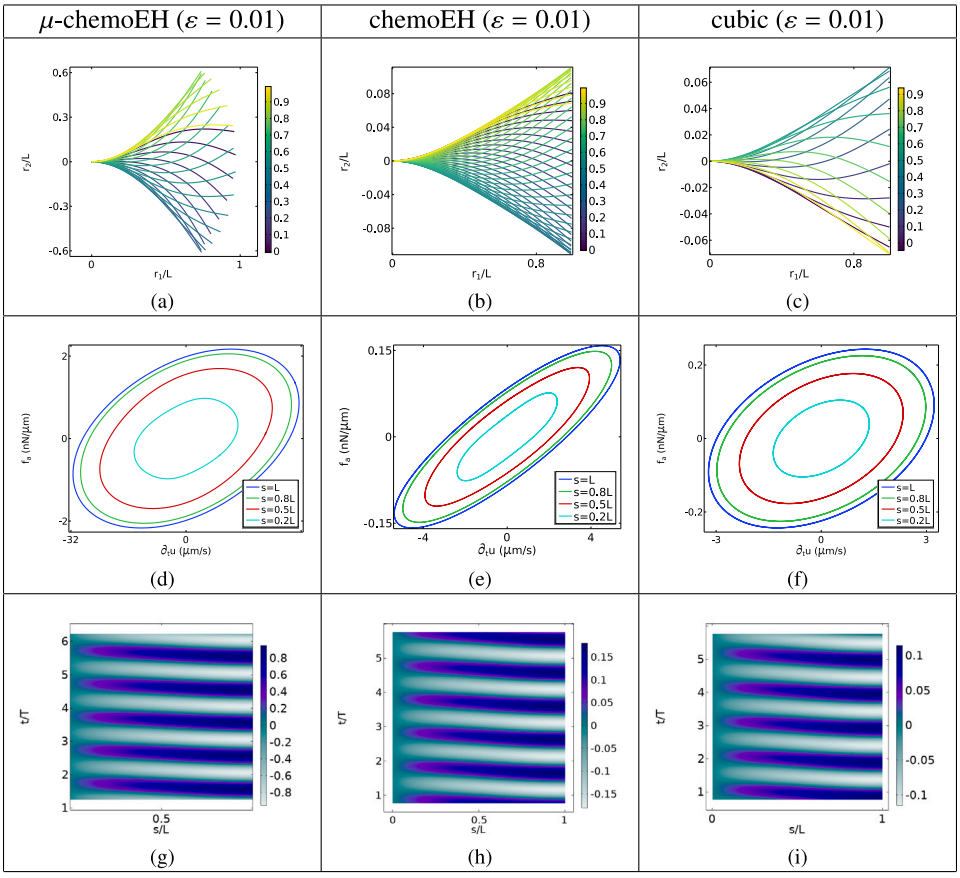

Fig. 7. Chlamydomonas flagella: comparison between three models at $\varepsilon = 0.01$: μ-chemoEH (first column), chemoEH model (second column), cubic-model (third column). For each model, we show the deformed configuration (first row), the limit cycles between active force and velocity at different arc-length (second row) and the kymograph of the tangent angle $\varphi(s,t)$ with the legend bar on the right showing its amplitude, s is normalized over L and t over a period T, (third row).

The deformed configurations plotted in Figs. 8(a) and 8(b) display some similarities in the curvature of the flagellum, while the filaments in Fig. 8(c) are less curved. We observe that, while in the μ-chemoEH and in the cubic model, the active force versus the sliding velocity curve remains roughly the same starting from half of the flagellum onward, in the chemoEH model the relation looks different depending on the distance from the base. In Fig. 8(e) we observe that the active force at the tip is twice the one of the rest of the flagella. As in the first group of simulations, near the bifurcation, the direction of the limit cycle is anticlockwise. With this set of parameters, the kymograph in the third row of Fig. 8 show interesting differences. While in the μ-chemoEH model we observe similar velocity and direction of propagation as in the case $\varepsilon = 0.01$, in the chemoEH we observe a change of wave propagation direction, from base to tip, and in the cubic model we recognize the emergence of standing waves. The frequency for the μ-chemoEH stays the same, leading us to notice that some of the linear information were retained by changing ε, probably because the system is still close to the bifurcation parameter. This is not the case for the other two models: in the chemoEH case, the frequency is $\theta = 40$ Hz, while for the cubic model, the frequency decreases to $\theta = 45.5$ Hz. Both the linear and nonlinear frequencies lie in the observable range given by Sartori et al. (2016), Mondal et al. (2020).

We now analyze the behavior of the μ-chemoEH model near the bifurcation. In Fig. 9(a) and (b), we plot the normalized tip amplitude as the distance from instability ε is varied for both the Chlamydomonas and the Bull Sperm. For every $s \in [0, L]$, we define the oscillation

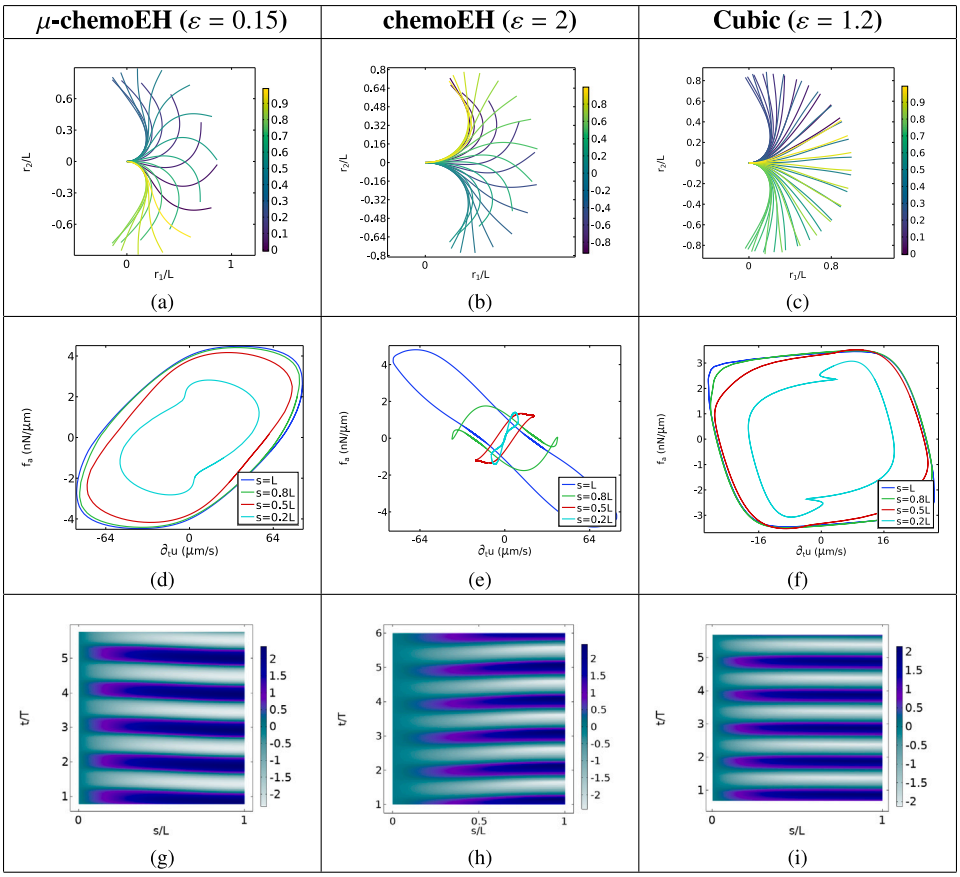

Fig. 8. Chlamydomonas flagella: comparison between three models in the nonlinear regime. Same as Fig. 7 but with $\varepsilon = 0.15$ for the μ-chemoEH, $\varepsilon = 2$ for the chemoEH model and $\varepsilon = 1.2$ for the cubic model.

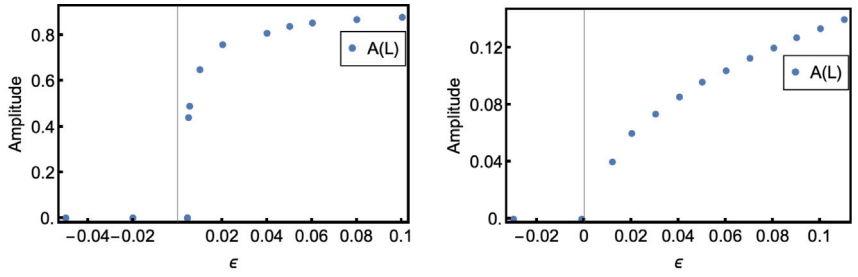

Fig. 9. Normalized amplitude $A(L)$ of the tip displacement against the distance ε from the instability. The amplitude (29) is plotted for the Chlamydomonas parameters (a) and for the Bull Sperm (b). The amplitude was measured when the oscillation reached its limit cycle, after $\bar{t} = 1.4$ s.

amplitude as

$$A(s;\varepsilon) = \frac{\max_{t>\bar{t}} r_2(s,t;\varepsilon) - \min_{t>\bar{t}} r_2(s,t;\varepsilon)}{2L}, \tag{29}$$

where $\bar{t}$ denotes a time elapsed after the solution has reached its limit cycle (defined empirically). We observe a sudden jump at the instability, with the amplitude reaching $A(L) = 0.44$, which may indicate the presence of a subcritical Hopf bifurcation. However, for longer flagella (Fig. 9(b)), the behavior clearly exhibits a supercritical bifurcation. This discrepancy suggests that the observed subcritical behavior might not be an intrinsic property of the μ-chemoEH model. In any case, this issue requires further investigation.

6.2. Tug of war

Using the parameters in Table 2, we compute $p^{\pm}$ and $q^{\pm}$ as in Eq. (15). These coefficients are then used to obtain the probabilities $P^{\pm}$ within a tug-of-war unit. The interaction between the motors and the filaments, governed by the potentials $\Delta W(\xi)$ generate forces defined as:

$$f^{\pm}_{\text{pot}}(\xi,t;s,\varepsilon) = P^{\pm}(\xi,t;s,\varepsilon)\partial_{\xi}\Delta W(\xi).$$

The ξ-averaged forces $f^{\pm}_{\text{pot}}$ over the tug-of-war cell are the motor force densities $f^{\pm}(t)$, introduced in Eqs. (8) and (9). The total active force is then:

$$f_a = \int_0^{\ell} \left(f^{+}_{\text{pot}}(\xi) - f^{-}_{\text{pot}}(\xi) \right) d\xi.$$

Fixing $t = 400$ ms and $s \in [0, L]$ we examine the system's behavior when ε varies. Fig. 10 illustrates this transition, showing the absolute values $|f^{+}_{\text{pot}}|$ and $-|f^{-}_{\text{pot}}|$. Arrows indicate the sign of forces $f^{\pm}_{\text{pot}}$: positive if pointing to the right and negative otherwise. Without loss of generality, we set $p_0 = 0$. At the steady state equilibrium, the forces $f^{\pm}_{\text{pot}}$

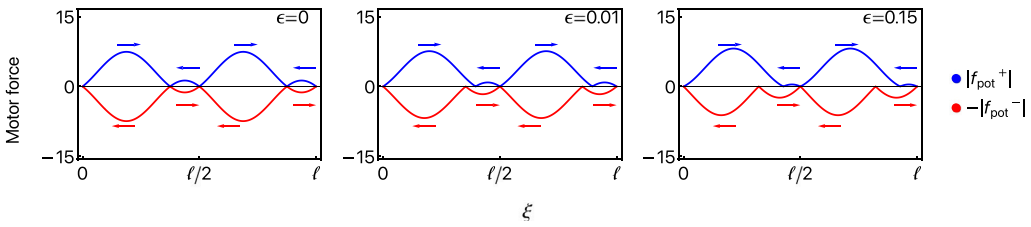

Fig. 10. Tug-of-war between two rows of motors as the bifurcation parameter ϵ varies, with arc length fixed at $s = 0.8L$. Forces $|f^{\pm}_{pot}|$ (blue and red) are shown with arrows indicating their sign. At equilibrium $\epsilon = 0$, the system is stalled, with equal and opposite forces. The central picture represents small amplitude oscillations emerging at $\epsilon = 0.01$, while the last picture shows the nonlinear regime of oscillations, at $\epsilon = 0.15$. Both of these graphs represent snapshots of the oscillations at fixed time $t = 400$ ms. In this case both small and large oscillation regimes show greater force on the upper filament than the lower. The nonlinear regime also exhibits the highest total active force. Parameters are as in Table 2. (For interpretation of the references to color in this figure legend, the reader is referred to the web version of this article.)

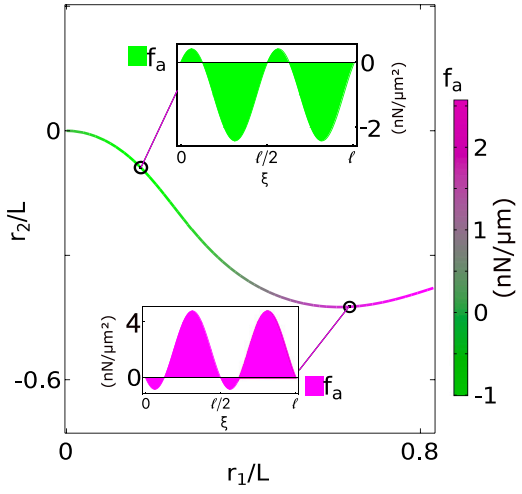

Fig. 11. Active force along the deformed configuration at $\epsilon = 0.15$ and time $t = 400$ ms. The color bar on the right depicts the active force f_a going from negative, in green, to positive, in magenta. The graphs of the force $f^{+}_{pot} - f^{-}_{pot}$ at $s = 0.2L$ and at $s = 0.5L$, respectively, are represented in the green and magenta inlets. The area under the graphs is the total active force f_a. (For interpretation of the references to color in this figure legend, the reader is referred to the web version of this article.)

are equal in magnitude but opposite in direction, implying that motors are stalled with equal stored potential energy. As the chemical energy increases, the forces show different magnitude, leading to a nonzero total active force. This imbalance drives filament sliding, as seen in the plots in Fig. 10 and leads to the so called tug-of-war scenario between motors anchored to opposite filaments. When $\epsilon = 0.15$, the system enters a nonlinear dynamic and oscillatory regime where one motor group dominates, generating a net active force.

Fig. 11 shows the deformed flagellum at $t = 200$ ms, colored to represent the active force $f_a(t, s)$ along its length. At $s_1 = 0.2L$ and $s_2 = 0.8L$, the active force have opposite signs. The inlets show the difference $f^{+}_{pot} - f^{-}_{pot}$, with areas under the curve representing $f_a(t, s_j)$ for $j = 1, 2$. Both Figs. 10 and 11 represent the system when the numerical solution has reached a limit cycle.

7. Discussion

In summary, we have formulated and solved a model coupling the mechanics of a two-dimensional flagellum with clamped–free boundary conditions with the fully nonlinear dynamics of molecular motors. Our model generalizes the two-state model introduced in Camalet and Jülicher (2000) and we have called this framework the μ-chemoEH model. The issue of having different length scales at play, the macroscopic one given by the filament, and the microscopic one ξ, is solved by computing the Fourier expansion for the binding probabilities of the motors. The μ-chemoEH is therefore reduced to a system of five ODEs for the sliding velocity and for only four Fourier coefficients of the probabilities. To obtain this reduction in the number of unknowns, we define both the transition rates and the potentials as cosine and/or sine functions, following Guérin et al. (2011b). In this way, we arrive at a system which is easily comparable with the chemoEH model (Oriola et al., 2017), from both theoretical and numerical perspectives. The two models present key differences in the hypothesis on the chemistry, in particular on the transition rates, which prevent us to derive the chemoEH model as a simple average of the μ-chemoEH one. We also discuss a third feedback mechanism derived as an approximation of the μ-chemoEH one, termed cubic model, which aligns with the model proposed in Hilfinger et al. (2009) in the frequency domain. The three models can be summarized as follows: the μ-chemoEH and chemoEH models describe molecular motor dynamics, linking attachment/detachment probabilities, velocity, and active force to oscillations. The μ-chemoEH operates at the microscopic spatial scale ξ, while the chemoEH operates with averages within a tug-of-war unit. The cubic model focuses solely on the relationship between active force and velocity, embedding microscopic details into the scalar coefficients governing the macroscopic flagellar dynamics.

Simulations confirmed that the μ-chemoEH effectively captures oscillatory behavior near the bifurcation point, which is to be expected since the linear response coefficient (26) is proportional to the one used in Camalet and Jülicher (2000). The novelty of the μ-chemoEH lies in its nonlinear component, which emerges from the product of the velocity times the Fourier coefficients of the probabilities, as one can appreciate in the ODE system (16).

The cubic model can be derived from the μ-chemoEH model by approximating the nonlinear components of the system in (16). A comparison of the two models, μ-chemoEH and cubic, highlights their differences in handling nonlinear components. The μ-chemoEH model allows for configurations that are nearly self-coiling under large waveform deformations, whereas the cubic model's nonlinearities restrict such behavior. Interestingly, when considering the isolated axoneme $f = 0$, the cubic model can be interpreted as a form of van der Pol oscillator for the velocity variable (Strogatz, 2015).

By comparing the three different models, using parameters for short flagella, it is possible to investigate the differences between the nonlinear models far from the bifurcation point by examining, for example, the active force against velocity graphs once the system has entered oscillation (Fig. 8). Notably, although the magnitudes of force and velocity are comparable across models, the limit cycles reveal that the distribution of active forces along the flagella varies. The two row-model could be an alternative for fitting the data from *Chlamydomonas* and to explore its implications in the case of large amplitude deformations.

Furthermore, our selected parameters indicate a change in the direction of the emerging traveling waves when moving away from the instability. While the μ-chemoEH model corroborates the existence of the retrograde (tip to base) traveling waves identified by the linear study, the chemoEH model demonstrates a reversal in the sign of propagation, with the waves propagating from base to tip. This propagation

is typical of curvature control model, at least in the linear regime (Bayly and Wilson, 2015).

We have also obtained feedback graphs (active force vs. velocity or active moment vs. curvature after the system reaches its limit cycle behavior) for the various models analyzed. These graphs are of great importance, since they can serve as a foundation for developing phenomenological models, just as in Gallagher et al. (2023), Brokaw (1975).

The μ-chemoEH model makes it possible to study what happens at the microscopic level in a tug-of-war unit by reconstructing the probabilities of detachment and attachment in their entirety. This provides us with a visual representation of the competition between the motors by calculating the active force in the $[0, \ell]$ segment. When the motors stall, non-zero forces oppose each other in sign and direction, creating a zero resultant. When the system receives enough ATP, one motor row prevails over the other, bringing the system out of equilibrium and causing oscillatory sliding between the filaments.

In conclusion, the μ-chemoEH model was based on the classical simplified model for the bending elasticity of the axoneme proposed in Camalet and Jülicher (2000). It fits within the family of nonlinear models based on sliding feedback and aims to describe, in as much detail as possible, the activity of the motors. In the context of a comprehensive elasto-hydrodynamic description of the flagellum, we focus on how the independent molecular motors synchronize and on how the forces generated by the motors coordinate to produce the macroscopic torques that drive the flagellum. It would be interesting to corroborate the finding of this study with experimental data and eventually to reduce the μ -chemoEH model to a reaction–diffusion model as the ones in Mondal et al. (2020), Cass and Bloomfield-Gadêlha (2023). Another line of investigation would be to couple the ODE given by the μ-chemoEH model with a three-dimensional model of the filament. Similar studies have been conducted in Sartori (2019), which used the curvature feedback model, and in Clarke et al. (2024), Ling et al. (2018), where the flagellum was subjected to an external distribution of compressive axial forces. These studies revealed the existence of a secondary bifurcation, in which the flagellum transitions from a spinning to a flapping dynamical configuration. Alternative and more detailed models for the axoneme will be considered in future work, starting from the one proposed in Cicconofri et al. (2021).

CRediT authorship contribution statement

Irene Anello: Writing – review & editing, Writing – original draft, Methodology, Formal analysis, Data curation, Conceptualization. **François Alouges:** Writing – review & editing, Methodology, Investigation, Conceptualization. **Antonio De Simone:** Writing – review & editing, Writing – original draft, Supervision, Methodology, Formal analysis, Conceptualization.

Declaration of competing interest

The authors declare that they have no known competing financial interests or personal relationships that could have appeared to influence the work reported in this paper.

Acknowledgments

We gratefully acknowledge the support by the European Research Council through ERC Advanced Grant MicroMotility (GA 340685) and ERC PoC Grant Stripe-o-Morph (GA 101069436). Additional support was provided by the Italian Ministry of Research through the projects Response (PRIN 2020) and Abyss (PRIN 2022).

Appendix A. On the μ-chemoEH model

A.1. Higher order terms

By substituting the Fourier expansion (15) in the PDE system (12), one gets an infinite number of ODEs systems, one for each $n \geq 0$.

For $n = 0$ we obtain two decoupled equations

$$\dot{p_0}^{\pm}(t) = -\alpha p_0^{\pm}(t) + \alpha\eta/\ell,$$

whose solution exponentially decay to η/ℓ for large times. For $n = 1$ we get (16), while for $n > 1$, we obtain

$$\begin{cases} \dot{p}_n^+(t) + \frac{2\pi}{\ell}\dot{u}(t)q_n^+(t) = -\alpha p_n^+(t), \\ \dot{q}_n^+(t) - \frac{2\pi}{\ell}\dot{u}(t)p_n^+(t) = -\alpha q_n^+(t), \\ \dot{p}_n^-(t) - \frac{2\pi}{\ell}\dot{u}(t)q_n^-(t) = -\alpha p_n^-(t), \\ \dot{q}_n^-(t) + \frac{2\pi}{\ell}\dot{u}(t)p_n^-(t) = -\alpha q_n^-(t) \end{cases} \tag{A.1}$$

The solutions $q_n^{\pm}$ and $p_n^{\pm}$ with $n > 1$ are completely determined by knowing $u(t)$, and they go to zero for large times, independently on the initial conditions. We therefore omit to explicitly solve this last system, and just consider $p_n^{\pm} = q_n^{\pm} = 0$ when $n > 1$.

A.2. Isolated axoneme

Now we study the isolated motor-filament systems for the ODE (16) by letting $f(t) = 0$. We focus on the linearized problem, while a comprehensive nonlinear analysis is carried out in Alouges et al. (2024). We rewrite the system as

$$\begin{cases} \dot{p}^+(t) = -\frac{2\pi}{\ell}\dot{u}(t)q^+(t) - \alpha p^+(t) + \alpha\Omega/(2\pi^2\ell), \\ \dot{q}^+(t) = \frac{2\pi}{\ell}\dot{u}(t)p^+(t) - \alpha q^+(t) + \alpha\Omega/(2\pi^2\ell), \\ \dot{p}^-(t) = \frac{2\pi}{\ell}\dot{u}(t)q^-(t) - \alpha p^-(t) + \alpha\Omega/(2\pi^2\ell), \\ \dot{q}^-(t) = -\frac{2\pi}{\ell}\dot{u}(t)p^-(t) - \alpha q^-(t) + \alpha\Omega/(2\pi^2\ell), \\ \dot{u}(t) = \frac{1}{2\lambda}\left(-2Ku(t) + \rho N\pi U\left(q^+(t) - q^-(t)\right)\right). \end{cases} \tag{A.2}$$

The Jacobian of this system, computed at the equilibrium point $p_{eq}^{\pm} = q_{eq}^{\pm} = \Omega/(2\pi^2\ell)$ and $u_{eq} = 0$, reveals five eigenvalues λ_i: the first three are negative, $\lambda_i = -\alpha$ for $i = 1, 2, 3$, while the other two are complex and conjugated $\lambda_{4,5} = \tau \pm i\omega$, where $\tau(\Omega) = -\frac{K}{2\lambda} - \frac{\alpha}{2} + \Omega\frac{U\rho N}{2\ell^2\lambda}$ and $\omega(\Omega) = \sqrt{\frac{K\alpha}{\lambda} - \tau^2(\Omega)}$.

Furthermore, there exist a critical ATP concentration value $\Omega_0 = \ell^2(K\alpha + \lambda)/(U\rho N)$ for which $\tau(\Omega_0) = 0$ and $\omega(\Omega_0) = \sqrt{\frac{K\alpha}{\lambda}} \neq 0$. In particular, by varying Ω, $\tau = \tau(\Omega)$ goes from negative to positive when crossing Ω_0. We are then in the right hypothesis to reduce the system (A.2) to a two-dimensional system that shows an Hopf-bifurcation around the equilibrium point and near Ω_0. We transform the system in such a way that the linear matrix associated to (A.2) becomes a block matrix. The transformation is the following: at first we bring the system to the origin

$$\delta p^{\pm} = p^{\pm} - p_{eq}^{\pm},\ \delta q^{\pm} = q^{\pm} - q_{eq}^{\pm},$$

then we write

$$r = \delta p^+ + \delta q^+ \quad s = \delta p^- + \delta q^-, \quad z = \tfrac{1}{2}(\delta q^+ + \delta q^-), \quad y = \tfrac{1}{2}(\delta q^+ - \delta q^-).$$

In this way, the linear part of the system (A.2) becomes

$$\begin{pmatrix} \dot{r} \\ \dot{s} \\ \dot{z} \end{pmatrix} = -\alpha \begin{pmatrix} r \\ s \\ z \end{pmatrix}, \quad \begin{pmatrix} \dot{y} \\ \dot{u} \end{pmatrix} = \frac{1}{\lambda}\begin{pmatrix} -\alpha\lambda + k_{cb}\Omega\rho N & -\frac{\Omega K}{\pi\ell^2} \\ \rho N\pi U & -K \end{pmatrix}\begin{pmatrix} y \\ u \end{pmatrix}$$

At the critical bifurcation point Ω_0 the variables r, s and z decay to their equilibrium point in time, while y and u oscillates around zero with frequency $\omega_0 = \omega(\Omega_0)$. This means that the pair (y, u) is the one that contributes to the Hopf-bifurcation. In order to recover the information for the original variables, we transform back the system

and get, at a linear level, that all the variables $p^{\pm}$, $q^{\pm}$ and u oscillate around their own equilibrium position with frequency ω_0.

In conclusion, while the ATP concentration is such that $\Omega \ll \Omega_0$, the motors are stalled at the equilibrium, which depends on Ω, and the filament does not move. In this regime, molecular motors are storing chemical energy, which is then converted it into mechanical work as soon as the ATP concentration becomes greater than the critical value Ω_0.

Appendix B. On the chemoEH model

We can compare the μ-chemoEH with the chemoEH by considering the last with zero force $f(t) = 0$

$$\begin{cases} \dot{n}^+ = \pi_0(N - n^+) - \varepsilon_0 e^{\bar{f}} n^+ e^{-\bar{f}\dot{u}/v_0} \\ \dot{n}^- = \pi_0(N - n^-) - \varepsilon_0 e^{\bar{f}} n^- e^{\bar{f}\dot{u}/v_0} \\ 0 = (n^+ - n^-) - (n^+ + n^-)\dot{u}/v_0 - \frac{K}{f_0\rho}u. \end{cases} \tag{B.1}$$

First, we observe that the equilibria are $n^{\pm}_{eq} = n_0 = \pi_0 N/\alpha_0$ and $u^{eq} = 0$, where $\alpha_0 = (\pi_0 + \varepsilon_0 e^{\bar{f}})$. We then apply two invertible transformations: first, defining $\delta n^{\pm} = n^{\pm} - n_0$, and subsequently, defining $z = (\delta n^+ + \delta n^-)/2$ and $y = (\delta n^+ - \delta n^-)/2$. After these transformations, the linearized system becomes

$$\dot{z} = -\alpha_0 z, \quad \begin{pmatrix} \dot{y} \\ \dot{u} \end{pmatrix} = \begin{pmatrix} -\alpha_0 + \varepsilon_0 e^{\bar{f}} \bar{f} & -\varepsilon_0 e^{\bar{f}} \bar{f} \frac{K}{2f_0\rho} \\ \frac{v_0}{n_0} & -\frac{K v_0}{2n_0 f_0 \rho} \end{pmatrix} \begin{pmatrix} y \\ u \end{pmatrix}. \tag{B.2}$$

When restricting the dynamics to the plane (y, u), we observe the onset of a Hopf bifurcation, as shown in Appendix A.2 for the μ-chemoEH system. In fact, the system has three eigenvalues: the first, $-\alpha_0$, is always negative, while the other two, $\lambda_{2,3} = \tau \pm i\omega$, are complex conjugates, where

$$\tau = -\left(\frac{K v_0}{2n_0 f_0 \rho} + \alpha_0 - \varepsilon_0 e^{\bar{f}} \bar{f} \right)$$

and

$$\omega = \sqrt{K\alpha_0 \frac{v_0}{2n_0 f_0 \rho} - \tau^2}.$$

Moreover, we observe that $\tau(f_0) = 0$ when

$$f_0 = v_0 \frac{K(\pi_0 + \varepsilon_0 e^{\bar{f}})}{2N\pi_0\rho(-\pi_0 + \varepsilon_0 e^{\bar{f}}(\bar{f} - 1))}.$$

In general, $\tau(f_0)$ changes sign as f_0 varies, making f_0 the bifurcation parameter of the system in this case. At the linear level, the two models are equivalent.

Appendix C. Numerical simulations methods

The governing equations are implemented with the finite element software COMSOL Multiphysics in the equation mode, using a time-dependent environment. For each model, the torque balance Eq. (5) is coupled with system (7), implemented via the weak form PDE and the ODE interface, respectively. The weak form of the torque balance equation reads

$$-B \int_0^L \varphi'(s,t)\alpha'(s,t)\, ds + \int_0^L (T(s,t) + af(s,t))\alpha(s,t)\, ds = 0,$$

where α is a test function with the same clamped–free boundary conditions as φ. The BDF solver is used for the time-stepping. A Newton algorithm is employed to iteratively solve the nonlinear algebraic system resulting from the finite element discretization at each time step. The direct solver MUMPS is chosen for the solution of the linearized system at each iteration.

Data availability

Data will be made available on request.

References

Alouges, F., Anello, I., DeSimone, A., Lefebvre-Lepot, A., Levillain, J., 2024. Some mathematical models for flagellar activation mechanisms. arXiv:2409.03506.

Bayly, P.V., Wilson, K.S., 2014. Equations of interdoublet separation during flagella motion reveal mechanisms of wave propagation and instability. Biophys. J. 107 (7), http://dx.doi.org/10.1016/j.bpj.2014.07.064.

Bayly, P., Wilson, K., 2015. Analysis of unstable modes distinguishes mathematical models of flagellar motion. J. R. Soc. Interface 12 (106), http://dx.doi.org/10.1098/rsif.2015.0124.

Brokaw, C.J., 1971. Bend propagation by a sliding filament model for flagella. J. Exp. Biol. 55 (2), http://dx.doi.org/10.1242/jeb.55.2.289.

Brokaw, C.J., 1975. Molecular mechanism for oscillation in flagella and muscle. Proc. Natl. Acad. Sci. 72 (8), http://dx.doi.org/10.1073/pnas.72.8.310.

Brokaw, C., 1985. Computer simulation of flagellar movement. VI. Simple curvature-controlled models are incompletely specified. Biophys. J. 48 (4), http://dx.doi.org/10.1016/S0006-3495(85)83819-4.

Camalet, S., Jülicher, F., 2000. Generic aspects of axonemal beating. New J. Phys. 2 (1), http://dx.doi.org/10.1088/1367-2630/2/1/324.

Cass, J.F., Bloomfield-Gadêlha, H., 2023. The reaction-diffusion basis of animated patterns in eukaryotic flagella. Nat. Commun. 14 (1), http://dx.doi.org/10.1038/s41467-023-40338-2.

Cicconofri, G., Noselli, G., DeSimone, A., 2021. The biomechanical role of extra-axonemal structures in shaping the flagellar beat of Euglena gracilis. Elife 10, http://dx.doi.org/10.7554/eLife.58610.

Clarke, B., Hwang, Y., Keaveny, E.E., 2024. Bifurcations and nonlinear dynamics of the follower force model for active filaments. Phys. Rev. Fluids 9, http://dx.doi.org/10.1103/PhysRevFluids.9.073101.

Gaffney, E.A., Gadêlha, H., Smith, D.J., Blake, J.R., Kirkman-Brown, J.C., 2011. Mammalian sperm motility: observation and theory. Annu. Rev. Fluid Mec. 43 (1), http://dx.doi.org/10.1146/annurev-fluid-121108-145442.

Gallagher, M.T., Kirkman-Brown, J.C., Smith, D.J., 2023. Axonemal regulation by curvature explains sperm flagellar waveform modulation. Proc. Natl. Acad. Sci. Nexus 2 (3), http://dx.doi.org/10.1093/pnasnexus/pgad072.

Geyer, V.F., Howard, J., Sartori, P., 2022. Ciliary beating patterns map onto a low-dimensional behavioural space. Nat. Phys. 18 (3), http://dx.doi.org/10.1038/s41567-021-01446-2.

Gray, J., Hancock, G.J., 1955. The propulsion of sea-urchin spermatozoa. J. Exp. Biol. 32 (4).

Grill, S.W., Kruse, K., Jülicher, F., 2005. Theory of mitotic spindle oscillations. Phys. Rev. Lett. 94 (10), http://dx.doi.org/10.1103/PhysRevLett.94.108104.

Guérin, T., Prost, J., Joanny, J.-F., 2011a. Bidirectional motion of motor assemblies and the weak-noise escape problem. Phys. Rev. E Stat. Nonlinear Soft Matter Phys. 84 (4), http://dx.doi.org/10.1103/PhysRevE.84.041901.

Guérin, T., Prost, J., Joanny, J.F., 2011b. Dynamical behavior of molecular motor assemblies in the rigid and crossbridge models. Eur. Phys. J. E 34, http://dx.doi.org/10.1140/epje/i2011-11060-5.

Heuser, T., Raytchev, M., Krell, J., Porter, M.E., Nicastro, D., 2009. The dynein regulatory complex is the nexin link and a major regulatory node in cilia and flagella. J. Chromatogr. B 187 (6), http://dx.doi.org/10.1083/jcb.200908067.

Hilfinger, A., Chattopadhyay, A.K., Jülicher, F., 2009. Nonlinear dynamics of cilia and flagella. Phys. Rev. E Stat. Nonlinear Soft Matter Phys. 79 (5), http://dx.doi.org/10.1103/PhysRevE.79.051918.

Howard, J., Chasteen, A., Ouyang, X., Geyer, V.F., Sartori, P., 2022. Predicting the locations of force-generating dyneins in beating cilia and flagella. Front. Cell Dev. Biol. 10, http://dx.doi.org/10.3389/fcell.2022.995847.

Jülicher, F., 1999. Force and motion generation of molecular motors: A generic description. In: Transport and Structure. http://dx.doi.org/10.1007/BFb0104221.

Jülicher, F., Ajdari, A., Prost, J., 1997. Modeling molecular motors. Rep. Math. Phys. 69 (4), http://dx.doi.org/10.1103/RevModPhys.69.1269.

Jülicher, F., Prost, J., 1995. Cooperative molecular motors. Phys. Rev. Lett. 75 (13), http://dx.doi.org/10.1103/PhysRevLett.75.2618.

Lauga, E., Powers, T.R., 2009. The hydrodynamics of swimming microorganisms. Rep. Progr. Phys. 72 (9), http://dx.doi.org/10.1088/0034-4885/72/9/096601.

Lin, J., Nicastro, D., 2018. Asymmetric distribution and spatial switching of dynein activity generates ciliary motility. Science 360 (6387), http://dx.doi.org/10.1126/science.aar1968.

Lindemann, C.B., 1994a. A "geometric clutch" hypothesis to explain oscillations of the axoneme of cilia and flagella. J. Theoret. Biol. 168 (2), http://dx.doi.org/10.1006/jtbi.1994.1097.

Lindemann, C.B., 1994b. A model of flagellar and ciliary functioning which uses the forces transverse to the axoneme as the regulator of dynein activation. Cell Motil. Cytoskeleton 29 (2), http://dx.doi.org/10.1002/cm.970290206.

Ling, F., Guo, H., Kanso, E., 2018. Instability-driven oscillations of elastic microfilaments. J. R. Soc. Interface 15 (149), http://dx.doi.org/10.1098/rsif.2018.0594.

Machin, K., 1958. Wave propagation along flagella. J. Exp. Biol. 35 (4), http://dx.doi.org/10.1242/jeb.35.4.796.

Mondal, D., Adhikari, R., Sharma, P., 2020. Internal friction controls active ciliary oscillations near the instability threshold. Sci. Adv. 6 (33), http://dx.doi.org/10.1126/sciadv.abb0503.

Moran, J., McKean, P.G., Ginger, M.L., 2014. Eukaryotic flagella: Variations in form, function, and composition during evolution. BioScience 64 (12), http://dx.doi.org/10.1093/biosci/biu175.

Oriola, D., Gadêlha, H., Casademunt, J., 2017. Nonlinear amplitude dynamics in flagellar beating. R. Soc. Open Sci. 4 (3), http://dx.doi.org/10.1098/rsos.160698.

Purcell, E.M., 1977. Life at low Reynolds number. Am. J. Phys. 45 (1), http://dx.doi.org/10.1119/1.10903.

Riedel-Kruse, I.H., Hilfinger, A., Howard, J., Jülicher, F., 2007. How molecular motors shape the flagellar beat. HFSP J. 1 (3), http://dx.doi.org/10.2976/1.2773861.

Sartori, P., 2019. Effect of curvature and normal forces on motor regulation of cilia. arXiv:1905.04138.

Sartori, P., Geyer, V.F., Scholich, A., Jülicher, F., Howard, J., 2016. Dynamic curvature regulation accounts for the symmetric and asymmetric beats of Chlamydomonas flagella. Elife 5, http://dx.doi.org/10.7554/eLife.13258.

Smith, E.F., Yang, P., 2004. The radial spokes and central apparatus: mechano-chemical transducers that regulate flagellar motility. Cell Motil. Cytoskeleton 57 (1), http://dx.doi.org/10.1002/cm.10155.

Strogatz, S.H., 2015. Nonlinear Dynamics and Chaos: With Applications to Physics, Biology, Chemistry, and Engineering, second ed. CRC Press, http://dx.doi.org/10.1201/9780429492563.

Velho Rodrigues, M.F., Lisicki, M., Lauga, E., 2021. The bank of swimming organisms at the micron scale (BOSO-micro). PLoS One 16 (6), http://dx.doi.org/10.1371/journal.pone.0252291.